Research Article *Open Access*

WM PUBLICATIONS

Journal of Pioneering Artificial Intelligence Research

ISSN: 3069-0846

DOI: doi.org/10.63721/26JPAIR0144

Dynamic Analysis of a Robot that Refuses to Tip Over

Carmen-Silvia Oprina*, Ciprian Racuciu, Lucian-Stefanita Grigore, Radu Moinescu and Marius-Nicolae Nebancea

Doctoral School Defense and Security Systems Engineering, Military Technical Academy Ferdinand I, Bucharest, Romania

Citation: *Carmen-Silvia Oprina, Ciprian Racuciu, Lucian-Stefanita Grigore, Radu Moinescu, Marius-Nicolae Nebancea (2026) Dynamic Analysis of a Robot that Refuses to Tip Over. J of Poin Artf Research 2(3), 1-17. WMJ-JPAIR-144*

Abstract

This study introduces a validated analytical-dynamic model for a 6×6 mobile platform designed for hazardous environments. Findings demonstrate that center-of-mass positioning dictates a trade-off between obstacle negotiation and dynamic stability. Increased tire contact area is shown to optimize maneuverability and energy efficiency on deformable soils by reducing ground pressure and subsidence. Experimental results confirm the platform's efficacy on low-bearing terrains. While identifying needs for optimized mass distribution and adaptive torque control, the study validates the model's reliability for autonomous, safety-critical applications.

***Corresponding author**: Carmen-Silvia Oprina, Doctoral School Defense and Security Systems Engineering, Military Technical Academy "Ferdinand I", Bucharest, Romania.

Submitted: 01.06.2026 **Accepted**: 05.06.2026 **Published**: 22.06.2026

Keywords: Wheeled Robot, Vehicle Dynamics, Terrain Mechanics, Motion Control, Autonomous System

Introduction

Terrestrial mobile robots are autonomous or teleoperated mechatronic platforms designed to operate in structured and unstructured environments, performing high-risk missions such as radiation detection, hazardous material handling, or environmental sampling in contaminated zones. By substituting direct human intervention, these systems enhance operational safety and reduce exposure to hazards, making them critical in military, industrial, and civil protection applications [1].

Designing and integrating such platforms entails significant challenges in mobility and stability, requiring coordination between propulsion, control, and communication subsystems and those dedicated to payload operations. Platform stability is strongly influenced by the center-of-mass (CG) location, payload distribution, and wheel or track characteristics, while mobility depends on the interaction between the propulsion mechanism and terrain, as well as the system's capacity to manage frictional variations,

inclinations, and obstacles [2, 3].

This study develops an analytical and dynamic model of a six-wheeled (6×6) mobile robot, validated experimentally through simulations and field tests. The work evaluates performance in ramp climbing, step-type obstacle traversal, and downhill braking. Integration of theoretical analysis with empirical measurements from rotation, current, and acceleration sensors enables rigorous correlation between the mathematical model and the robot's real-world behavior under high-risk operational scenarios.

Part of the RTTSERG platform architecture and preliminary experimental setup were previously reported in [4]. The present work extends the dynamic modeling framework and provides additional simulation and validation scenarios, as well as detailed analyses of the software, payload transport, and propulsion subsystems.

Related Work

Dynamic and traction models for off-road vehicles have been developed through rigorous theoretical approaches, where tire-terrain interaction is characterized for both rigid wheels and complex suspension systems. Wong established the foundational terramechanics framework for off-road vehicles, providing analytical formulations for rolling resistance, ramp climbing behavior, and adhesion losses, while Takács and Stépán analyzed the effects of tire contact patch memory on lateral vibrations in four-wheeled vehicles, emphasizing the role of load distribution and contact characteristics in lateral stability [2, 3, 5].

In the context of autonomous navigation and control for 6×6 mobile platforms, recent research has addressed both dynamic modeling and trajectory planning algorithms. Yu et al. proposed a dynamic modeling methodology for all-wheel-drive wheeled vehicles, with experimental validation demonstrating strong correlation between theoretical predictions and observed field behavior [6]. Complementarily, Wang and Liu explored fuzzy logic-based path planning for mobile robots in unknown environments, highlighting the importance of sensor integration and adaptive algorithms in maintaining stability and operational efficiency [7].

Studies on stability and obstacle traversal for 6×6 vehicles have underscored the critical influence of geometric parameters and center-of-gravity (CG) positioning on rollover avoidance and traction optimization. Tavoosi et al. investigated the vertical dynamics of a 6×6 robot, illustrating the correlation between load distribution and ground reaction forces during ramp ascent and descent [8]. Similarly, Appelqvist et al. examined the mechatronic design of autonomous military ground vehicles, emphasizing the significance of modular architectures and integrated control systems in negotiating complex terrain and obstacles. These works provide a robust theoretical framework for the modeling and experimental evaluation of the 6×6 mobile robot considered in this study [9].

Kinematics and Dynamics of Rttserg

The present section extends the dynamic modeling framework, providing additional formulation for simulation and experimental validation. The modeling of the 6×6 mobile terrestrial robot is formulated within the framework of the MultiBody Systems (MBS) theory, in which the mechanical structure is represented by an assembly of rigid bodies interconnected by joints and geometric and dynamic constraints, and the rolling environment is considered an external system that interacts through contacts and mechanical reactions (Fig. 1). The MBS approach allows the formal description of the kinematic and dynamic behavior of the platform, constituting the foundation for the analysis of mobility, stability and motion control, according to established paradigms in mobile and terramechanical robotics [1-3].

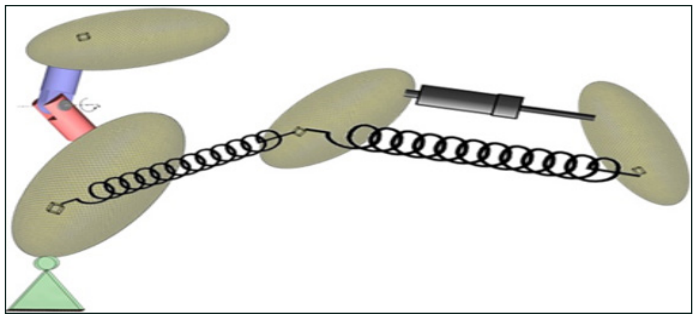

Figure 1: MBS – schematic of an open kinematic chain [1].

Kinematic analysis starts from the definition of position vectors and coordinate transformations between the inertial system and the local frames attached to the robot bodies (Figure 2).

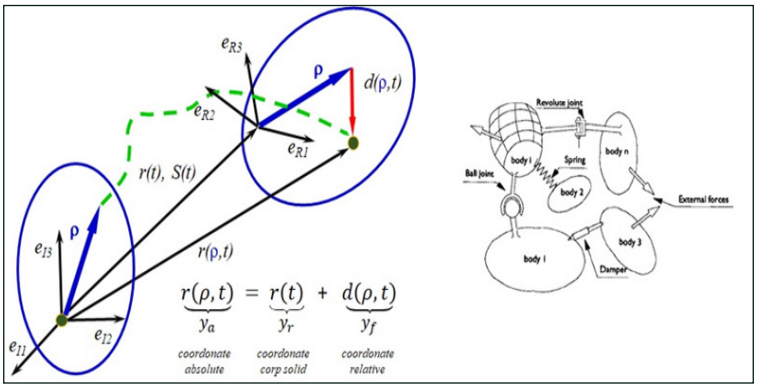

Figure 2: MBS – transformation from the global coordinate frame to a local (partial)17 coordinate frame [1].

The position and orientation vectors allow the derivation of generalized velocities and accelerations, providing the basis for the formulation of the equations of motion and for the development of navigation and control algorithms. For the 6×6 robot without steering wheels, the kinematic model is formulated in a two-dimensional (2D) plane, under simplifying assumptions regarding geometric symmetry, neglect of secondary friction effects and restriction of independent lateral motion, leading to a non-holonomic system characteristic of wheeled vehicles. The general equation of motion of the center of mass is expressed by:

$$\dot{X}_{CG} \cdot \cos\psi + \dot{Y}_{CG} \cdot \sin\psi = \nu \tag{1}$$

were (X_{CG}, Y_{CG}) are the coordinates of the center of mass ψ is the orientation angle, and ν is the longitudinal velocity. The introduction of pseudo-velocities leads to the set of non-holonomic constraints:

$$\begin{cases} \delta_f = -\dot{X}_{CG} \cdot \sin\psi + \dot{Y}_{CG} \cdot \cos\psi \\ \delta_s = \dot{\psi} \end{cases} \tag{2}$$

from which the explicit kinematic equations of the platform result:

$$\begin{cases} \dot{X}_{CG} = \dot{Y}_{CG} \cdot \cos\psi - \delta_f \cdot \sin\psi \\ \dot{Y}_{CG} = \nu \cdot \sin\psi + \beta_f \cdot \cos\psi \\ \dot{\psi} = \delta_s \end{cases} \tag{3}$$

These relationships constitute the foundation of navigation modeling and trajectory control for non-holonomic mobile platforms.

The tire-terrain interaction introduces elastic and hysteresis phenomena, which require the use of advanced formulations based on partial differential equations to describe the spatiotemporal distributions of deformations in the contact patch (Fig. 3). The deformations of the front and rear tires are described by:

$$\begin{cases} \dot{p}_f(X_f,t) = -\delta_s - (l + e + X_f) \cdot \delta_r - p'_f(X_f,t) \cdot \dot{X}_f \\ \dot{p}_r(X_r,t) = -\delta_s - (l + e + X_r) \cdot \delta_r - p'_r(X_r,t) \cdot \dot{X}_r \end{cases} \tag{4}$$

where p_f, p_r represent the tire deformations, and δ_s, δ_r are pseudo-velocities associated with the kinematic constraints.

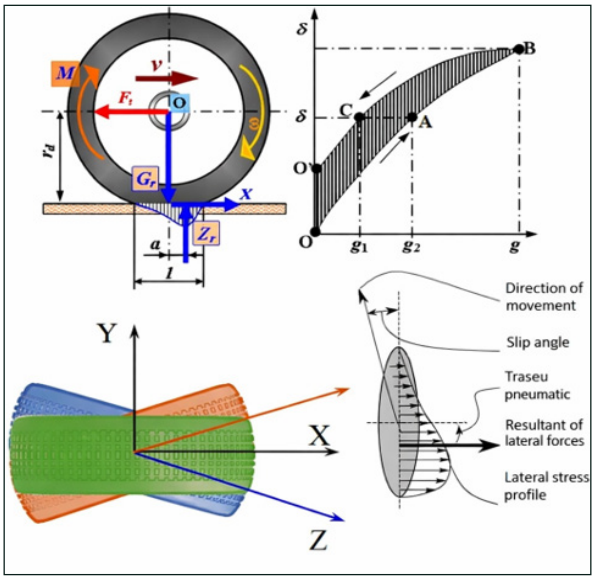

Figure 3: Representation of the wheel-road interaction.

The direct kinematics of the 6×6 robot is formulated by the transformation between the inertial frame and the mobile frame attached to the platform, described by:

$$\begin{bmatrix} \dot{x} \\ \dot{y} \\ \dot{\theta} \end{bmatrix} = \begin{bmatrix} \cos\theta & -\sin\theta & 0 \\ \sin\theta & \cos\theta & 0 \\ 0 & 0 & 1 \end{bmatrix} \cdot \begin{bmatrix} V_x \\ V_y \\ \omega_z \end{bmatrix} \tag{5}$$

and the relationship between the angular velocities of the wheels and the generalized velocities of the platform is:

$$\begin{bmatrix} V_x \\ V_y \\ \omega_z \end{bmatrix} = f \cdot \begin{bmatrix} \omega_I \cdot r \\ \omega_E \cdot r \end{bmatrix} \tag{6}$$

For planar motion with $V_y = 0$, the simplified relations are obtained:

$$\begin{cases} V_x = \dfrac{\omega_I \cdot r + \omega_E \cdot r}{2} \\ \omega_z = \dfrac{-\omega_I \cdot r + \omega_E \cdot r}{2 \cdot y_0} \end{cases} \tag{7}$$

and the turning radius is:

$$R = \frac{V_x}{\omega_z} = \lambda \cdot y_0 \tag{8}$$

$$\lambda = \frac{V_I + V_E}{-V_I + V_E} \tag{9}$$

These relationships highlight the direct link between the difference in side wheel speeds and the platform's

maneuverability, being consistent with the skid-steering and terremechanic theories of mobile vehicles [2, 6].

The dynamic model is formulated through the equilibrium equations of the forces and moments applied to the platform in plane motion:

$$\begin{cases} \sum F_x - R_x - m \cdot \frac{v_{CG}^2}{R} \cdot \sin\beta = 0 \\ \sum F_y = m \cdot \frac{v_{CG}^2}{R} \cdot \cos\beta \\ M_d - M_r = 0 \end{cases} \quad (10)$$

where the longitudinal and lateral forces of each wheel are determined by the tire-terrain interaction, and M_d and M_r represent the engine torque and the total resistive moment.

The tangential stress at the wheel-ground contact is modeled by the nonlinear relationship:

$$\tau = p \cdot \mu \cdot \left(1 - e^{-\frac{j}{k_\gamma}}\right) \quad (11)$$

which describes the shear behavior of the soil as a function of the relative deformation, according to classical theories of earth mechanics [3, 10]. The longitudinal and lateral forces are obtained by integrating the shear stresses on the contact patch:

$$F_x = \iint p \cdot \mu \cdot \left(1 - e^{-\frac{j}{k_\gamma}}\right) \cdot \sin(\pi + \omega_\gamma) \cdot dx \cdot dy \quad (12)$$

$$F_y = \iint p \cdot \mu \cdot \left(1 - e^{-\frac{j}{k_\gamma}}\right) \cdot \cos(\pi + \omega_\gamma) \cdot dx \cdot dy \quad (13)$$

where j represents the relative displacement, and ω_γ is the angular velocity of the wheel.

The integration of kinematic and dynamic models allows for the direct correlation of control variables with the overall mechanical behavior of the platform, providing a unified framework for simulation, control and experimental validation.

Overall Architecture of the Rttserg Robot

The overall architecture of the RTTSERG ground robot is structured around integrated hardware and functional components required to accomplish perception, planning, mission execution, communication, and navigation processes (Fig. 4). The perception component comprises the suite of sensors and data acquisition technologies. In this domain, universally standardized metrics and generalized comparative evaluation procedures are not yet established; therefore, implemented solutions remain largely application-dependent and rely on dedicated calibration and validation methodologies [11].

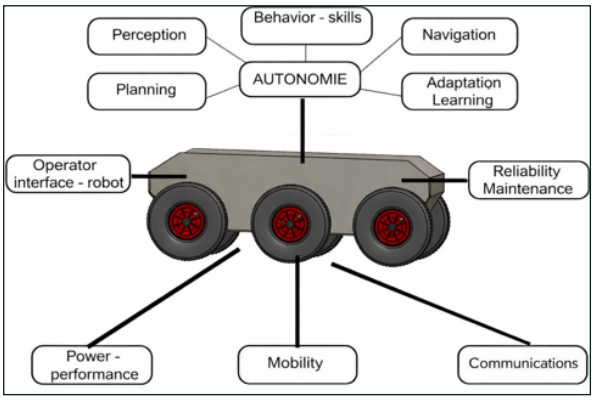

Figure 4: Representation of the UGV hardware components (adapted from Fig. ES-1, pg. 4).

Path planning represents the process of generating an optimal trajectory between an initial position and a target position under obstacle avoidance constraints. Planning algorithms treat traversable regions as admissible states and obstacles as constraints, constructing feasible trajectories between start and goal configurations. At a higher abstraction level, the mission management component encompasses the definition of operational objectives, constraints, and execution procedures, including compliance with legal regulations governing autonomous ground vehicle operation.

The communication subsystem is critical for robot functionality, particularly in teleoperated and autonomous modes. In teleoperation, the communication channel is embedded within the control loops linking sensors, actuators, and the human operator, thus requiring high bandwidth, low latency, and high reliability. Connectivity disruptions may result in loss of control over the platform. For wireless implementations, the employed technologies must reach an adequate Technology Readiness Level (TRL≥6), while performance is influenced by electromagnetic interference and Non-Line-of-Sight (NLOS) propagation conditions.

Navigation emerges from the integration of perception, planning, and communications, employing advanced localization, state estimation, and motion control techniques to ensure robust autonomous mobility in complex and dynamic environments.

Modular Hardware Architecture

The hardware architecture of the RTTSERG robot is modular, allowing each functional subsystem – perception, planning, mission management, communication, and navigation – to be developed, replaced, or upgraded independently without compromising the overall platform integrity (Fig. 5). This modular structure enables flexible integration of sensors and actuators, rapid adaptation to diverse operational requirements, and scalability of robotic capabilities while preserving hardware-software interoperability.

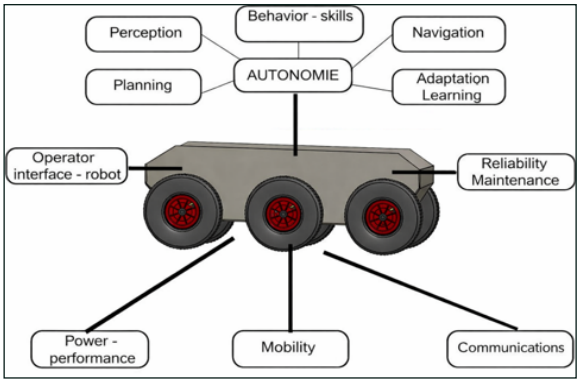

Figure 5: Representation of the UGV hardware architecture. [12]

The unmanned ground vehicle (UGV) is organized into distinct subsystems: locomotion, power supply, positioning, sensing, navigation, motion control, communications, human-machine interface (HMI), mission control, and payload control. This integrated modular architecture facilitates rapid adaptation to operational demands and ensures the performance required for mission deployment in dynamic environments.

RTTSERG Control System

The RTTSERG controller manages navigation and mission execution through a hybrid global-local path planning strategy. Global planning assumes prior knowledge of the environment and considers terrain as static, whereas local planning relies on real-time sensory input and is suitable for partially known or unknown environments [7, 13].

In the present implementation, RTTSERG operates in teleoperation mode; however, the perception subsystems continuously acquire environmental data for motion monitoring and adjustment. GPS integration is essential for operation in unstructured environments, while the incorporation of Machine Learning and Deep Learning techniques is critical for

advanced trajectory planning and enhanced operator safety.

Controllers are implemented using Commercial Off-The-Shelf (COTS) components, ensuring flexibility and cost efficiency. The integration of the information flow between the command station, the main controller, and the Ground Control Station (GCS) provides a robust framework for operational coordination and monitoring [9, 14].

Sensors Integrated on the RTTSERG Platform

The RTTSERG platform integrates a suite of sensors optimized for precise control and autonomous navigation.

Dual-channel Hall encoders measure the rotational speed of the traction motor shafts. Quadrature functionality allows for the determination of the direction of rotation and the calculation of the angular velocity, with a basic resolution of 64 pulses per revolution, subsequently multiplied by the reduction ratio of the reducer. These sensors are the essential element for implementing closed-loop control of speed and position.

The ACS712 current sensor continuously monitors the current consumption of the motors, a value directly proportional to the developed torque. The data obtained facilitates energy management, system protection and the application of advanced current-feedback control strategies.

The ADXL335 accelerometer provides triaxial acceleration measurements in the range of ±3g, characterized by low noise and very low power consumption (320µA). Inertial information is used for platform stabilization, trajectory correction, and inertial navigation support.

The RPLIDAR A1 2D laser scanner performs a full 360° scan of the environment up to a distance of 6 meters, with a frequency of 5.5Hz and an accuracy of better than 1%. The generated point cloud is exploited in SLAM algorithms for mapping, precise localization, and obstacle avoidance in real time.

Communication Subsystem

For teleoperation and data transmission, the platform uses Wi-Fi modules based on the ESP8266 chipset. The WI07C module transmits sensor data to a server via TCP/IP communication. Logical level adaptation (5 V to 3.3 V) is required to ensure module protection. Two identical Wi-Fi systems are employed-one installed on the robot and one at the operator station-providing a bidirectional channel for control commands and telemetry exchange.

Robot Control System

The control system is based on encoder feedback to maintain desired velocity under both level and inclined terrain conditions. The 6×6 platform is modeled as a non-holonomic system, with robot-terrain interaction characterized by propulsion, adhesion, cohesion, and support forces.

Geometric configuration significantly influences mobility and stability. The modeling framework accounts for terrain reaction forces, substrate characteristics, and external dynamic disturbances, ensuring accurate representation of system behavior during operation in complex environments.

Software Vector Transport Payload

The software subsystem of the payload transport vector is implemented on an Arduino microcontroller platform, using the open-source Arduino IDE development environment. The choice of this solution is based on the principles of modular embedded architectures and the use of COTS components, which allow rapid prototyping, code portability and easy integration with the hardware subsystems of the mobile robot. The controller is configured in slave mode, communicating with the higher control level through a dedicated serial protocol, which ensures a clear separation between the decision level and the execution level, according to the hierarchical control paradigm used in mobile robotic systems.

Initializing the controller involves configuring the output pins for driving the traction motors, setting the serial communication parameters, and initializing the I2C bus for interfacing with the power management subsystem. In this context, the control pins are organized into two independent channels, corresponding to the left and right motors, each channel using a power control pin (PWM) and a direction control pin. This structure reflects a classic differential control model of a wheeled land vehicle, frequently used in the literature on non-holonomic mobile robots.

The communication between the command station

and the on-board controller is carried out through a custom serial protocol (SerMesProtocol), based on start and end frame delimiters (STX/ETX), master-slave identifiers and explicit message length fields. This approach allows for transmission error detection, data packet integrity validation and subsequent protocol extension for additional functions. The main execution flow is implemented in the loop, which handles the reception of messages, validation of their structure and delegation of processing to a command semantic interpretation function.

The message processing function maps the received functional codes to the corresponding subroutines, according to a command dispatch mechanism. This structure allows a clear separation between the communication logic and the actual control logic, facilitating formal verification and modular testing of the software. The implemented commands include both kinematic control actions and energy state queries (charge level, voltage, current, temperature), reflecting the functional integration between the locomotion and energy subsystems.

Motor control is achieved through a dedicated function that interprets speed commands as two bytes, one for each motor. The numerical domain of the commands is divided into two distinct regions, corresponding to the forward and reverse directions of rotation, which allows the simultaneous encoding of the modulus and direction in a single command variable. This strategy is frequently used in embedded DC motor control systems and allows for efficient use of the communication channel bandwidth.

The code snippet corresponding to the initialization and main loop illustrates this software architecture (Fig. 6):

```
#include <Wire.h>

#include "BoardParams.h"

void setup(void) {
  pinMode(PIN_PWM_R, OUTPUT);
  pinMode(PIN_PWM_L, OUTPUT);
  pinMode(PIN_MOT_R, OUTPUT);
  pinMode(PIN_MOT_L, OUTPUT);
  pinMode(PIN_LED, OUTPUT);
  Serial.begin(BAUD_RATE);
  Wire.begin();
}
```

Figure 6: Source code snippet

The energy status monitoring is achieved by interfacing, via the I2C bus, with a fuel gauge module, using standardized commands to read electrical parameters. The ReadBatParam function implements a sequential access mechanism to the module's internal registers, including support for subcommands dedicated to reading instantaneous current. This approach is consistent with System Health Management models, where energy parameters are integrated into the decision loop to prevent performance degradation or system failure.

To avoid overloading the main loop and to distribute I2C operations over time, the reading of energy parameters is performed cyclically, on successive iterations of the execution loop. This strategy reduces the system response latency and minimizes interference between serial and I2C communication, contributing to the temporal stability of the embedded system.

The transmission of responses to the higher control level is achieved through a data publishing function, which reconstructs the communication frame according to the defined protocol and transmits both the functional code and the associated data. The explicit structuring of messages facilitates the integration of the controller into a wider distributed system, allowing interoperability with control stations developed in different software environments.

Rtserg Simulation

The numerical validation of the equations describing the dynamics of the carrier vector was carried out through simulations in the RTSERG environment, analyzing two critical scenarios for the evaluation of mobility performances: climbing a longitudinal ramp and crossing a step-type obstacle. These scenarios represent limit cases for the longitudinal and vertical stresses of the mobile platform and are relevant for applications in natural and industrial environments with variable terrain structure.

For movement on a ramp with longitudinal inclination angle α, the total weight of the robot G_a is decomposed into components parallel and normal to the contact surface. defined by $R_p = G_a \sin \alpha$[N], $R_r = G_a \cos \alpha$, where R_p represents the active or resistive component depending on the direction of travel, and R_r determines the distribution of normal reactions at the wheel level.

The total resistance force when climbing a ramp is modeled by the relationship:

$$R_\psi = R_p + f \cdot R_r = G_a \cdot (\pm \sin\alpha + \mathrm{f} \cdot \cos\alpha) \quad (14)$$

where f is the rolling resistance coefficient. The model additionally includes starting resistance, which reflects the contribution of the inertia of the rotating masses, expressed by

where f is the rolling resistance coefficient. The model additionally includes starting resistance, which reflects the contribution of the inertia of the rotating masses, expressed by

$$R_d = \delta \cdot \frac{G_a}{g} \cdot \frac{\mathrm{d}v}{\mathrm{d}t} \quad (15)$$

and aerodynamic drag

$$R_a = K \cdot A \cdot v_a^2 \quad (16)$$

where $K = 0.6125 \cdot c_x$ is the aerodynamic coefficient, A the frontal area, and va the relative air velocity. Although the aerodynamic contribution is small for the speed regime of land robots, its inclusion ensures the consistency of the model with classical theories of land vehicle dynamics.

Ramp Climbing Simulation

The performance when climbing the ramp was evaluated based on a kinematic-dynamic model that considers the robot mass m, the traction force F_t, the normal reactions F_N, the position of the center of mass (L_{CG}, h_{CG}) and the wheelbase L. The distribution of loads on the axles is determined by

$$F_N = \frac{m \cdot g \cdot (L_{CG} \cdot \cos\alpha + h_{CG} \cdot \sin\alpha)}{L} \quad (17)$$

and the required traction force is

$$F_t = \frac{m \cdot g \cdot r_m \cdot (\sin\alpha + f \cdot \cos\alpha)}{6} \quad (18)$$

where r_m is the radius of the wheels. The corresponding traction moment is

$$M_t = \frac{m \cdot g \cdot r_m \cdot v_a \cdot (\sin\alpha + f \cdot \cos\alpha)}{6} \quad (19)$$

The minimum adhesion condition for full exploitation of traction force is expressed by

$$\mu \geq \frac{L \cdot \sin\alpha}{h_{CG} \cdot \sin\alpha + L_{CG} \cos\alpha + L \cdot \cos\alpha} \quad (20)$$

and the critical angle of overturning is

$$\alpha = \arctan\left(\frac{L - L_{CG}}{h_{CG}}\right) \quad (21)$$

The numerical results, presented in Fig. 7 and Fig. 8, highlight the nonlinear increase in traction moment and

adhesion requirements with increasing ramp angle, confirming the consistency of the model with classical theories of land vehicle traction and validating its applicability for evaluating the climbing capacity of the mobile platform.

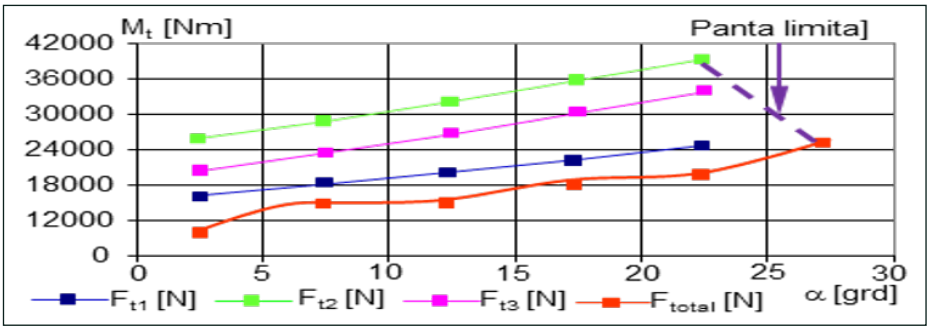

Figure 7: Variation of the required driving torque during uphill motion, without the radiation-testing equipment.

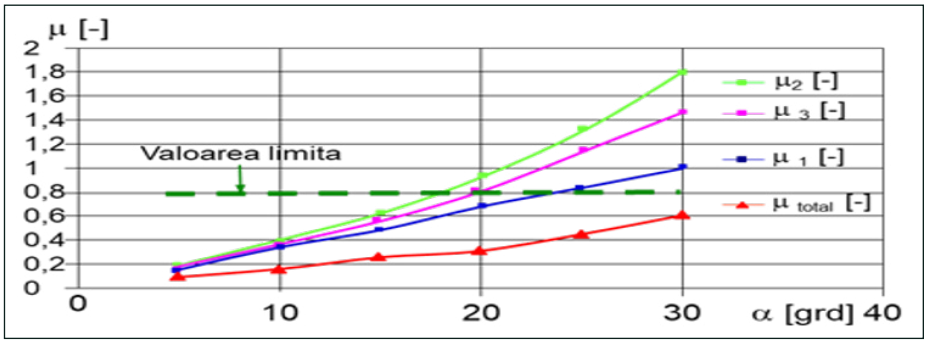

Figure 8: Variation of the required driving torque as a function of ramp inclination angle, under the same conditions, without the radiation-testing equipment.

Simulation of Crossing the Step Obstacle

The crossing of a step-type obstacle was analyzed for two limiting scenarios: (i) approaching the obstacle with the front axle and (ii) simultaneous approaching with two axles, in which case stability and distribution of traction efforts are favorable. The model considers the platform geometry, the position of the center of mass and the wheel-obstacle interaction through the longitudinal tilt angle β.

The geometric and equilibrium conditions are expressed by the relations

$$\mu \cdot d = r_m \cdot \sin\beta + x_G \cdot \cos\beta - y_G \cdot \sin\beta \quad (22)$$

$$\mu \cdot h = r_m - r_m \cdot \cos\beta + d \cdot \sin\beta \quad (23)$$

$$d = \frac{(h - r_m + r_m \cdot \cos\beta)}{\sin\beta} \quad (24)$$

$$\mu = r_m \cdot \sin\beta + d \cdot \cos\beta \quad (25)$$

where x_G and y_G are the coordinates of the center of mass, h is the height of the step, and d is the geometric distance between the contact point and the edge of the obstacle. The numerical results, illustrated in Fig. 9 and Fig. 10, highlight the significant increase in the friction coefficient and the required traction force with

increasing obstacle height, indicating the operational limits of the mobile platform.

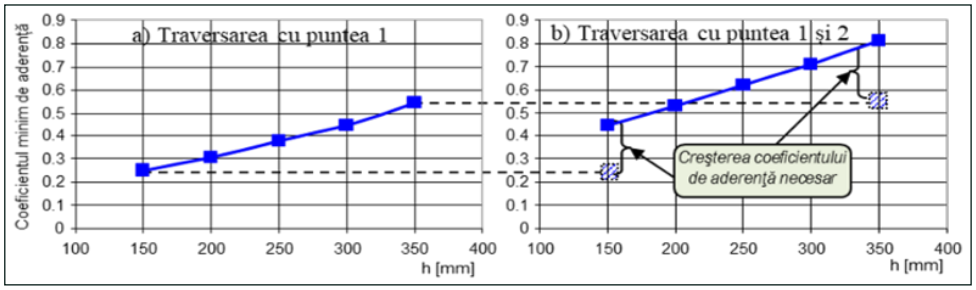

Figure 9: Variation of the required torque for obstacle crossing as a function of obstacle height.

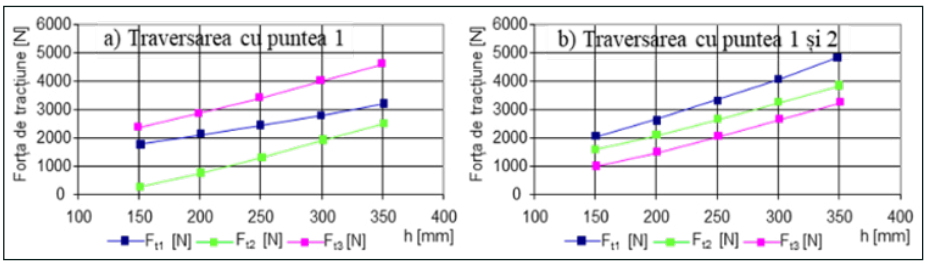

Figure 10: Variation of the required torque for obstacle crossing as a function of obstacle height.

The geometric and dynamic parameters used in the simulation are summarized in Table 1, including the wheel radius, wheelbase, center of mass position, and total robot mass, forming the basis for numerical and experimental validation.

Wheel radius r_m [mm]	130.00
Wheelbase L[mm]	400.00
Distance between front axle and center of gravity L_CG [mm]	200.00
Height of center of gravity from track h_CG [mm]	125.00
Mass of unequipped robot m[kg]	35.00
Adhesion coefficient μ[-]	0.8

Table 1: Robot characteristics used for simulation.

Analysis of Downhill Braking and Longitudinal Stability

The stability of the 6×6 platform in dynamic mode is critical during braking on longitudinal slopes, where deceleration induces load transfer to the front axle and displacement of the center of pressure. In the limit, for the misalignment $x = L - L_{CG}$, the maximum deceleration is given by

$$a = g \cdot \left(\frac{L - L_{CG}}{h_{CG}} \cdot \cos\alpha - \sin\alpha \right) \quad (26)$$

and for the case of wheel lock braking or regenerative electric braking, the relationship reduces to

$$a = g \cdot \left(\frac{L - L_{CG}}{h_{CG}} \right) \quad (27)$$

The analysis highlights that increasing the height of the center of mass or moving it towards the front reduces the maximum allowable deceleration and increases the risk of overturning, the result being consistent with the theories of dynamic load transfer in land vehicles. The analytical-numerical results are presented in Fig. 11, and the experimental validation, carried out by filtered accelerometric measurements and derivation of the velocity signal, is illustrated in Fig. 12 and Fig. 13. The agreement between the model and the experimental

data confirms its relevance for implementation in software algorithms for autonomous navigation and dynamic control of the stability of the mobile platform.

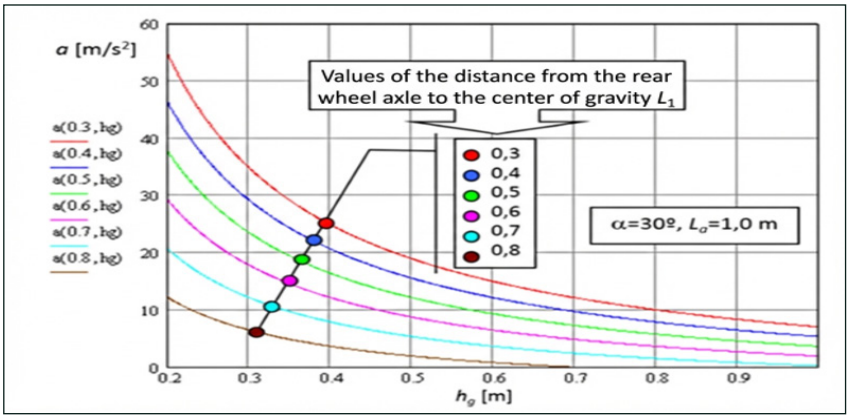

Figure 11: Variation of maximum deceleration when braking on a 30° slope as a function of CG position

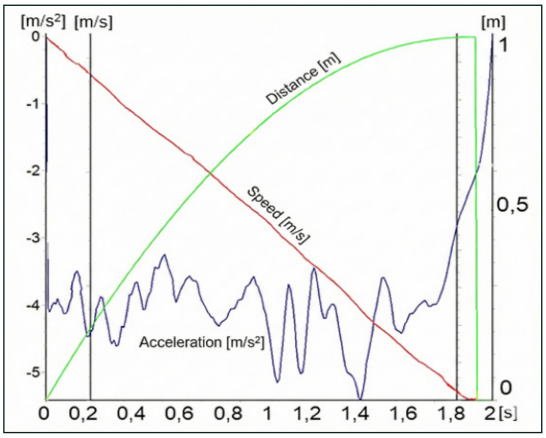

Figure 12: Dynamic characteristics of the 6×6 robot during slope braking

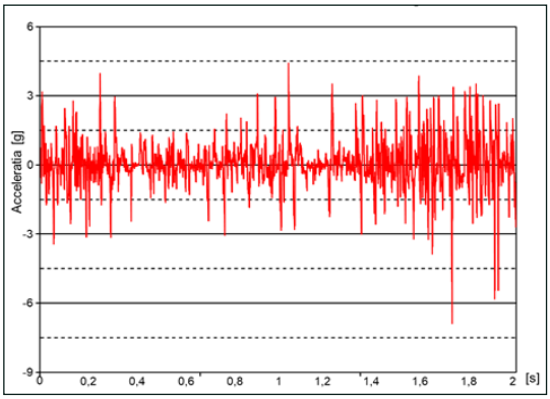

Figure 13: Longitudinal acceleration profile during downhill braking

Experimental Evaluation of Propulsion Dynamics in Risk-Critical Operating Conditions

To evaluate the dynamic behavior of the propulsion system under potentially hazardous conditions, an experimental bench dedicated to investigating the dynamic response of a traction actuator in controlled mode was developed. In a first stage, the experimental architecture included a single DC motor, a power driver (ESC), an Arduino Mega controller, an incremental encoder for speed measurement, a current sensor and a data acquisition system on a laptop, powered by a dedicated battery. This configuration allowed the analysis of speed control and the variation of traction torque as a function of load and command, constituting the basis for extrapolating the behavior to the complete 6×6 platform configuration.

The motor driver was interconnected with the Arduino Mega board through PWM channels and digital inputs for direction and speed control, ensuring a common ground reference between the controller, driver and power supply. The traction motor was connected to the dedicated outputs of the driver, and the incremental encoder was integrated into a measurement chain for speed monitoring, according to the scheme illustrated in Fig. 14. This architecture allows the implementation of closed-loop speed control, according to the classical principles of electromechanical control systems.

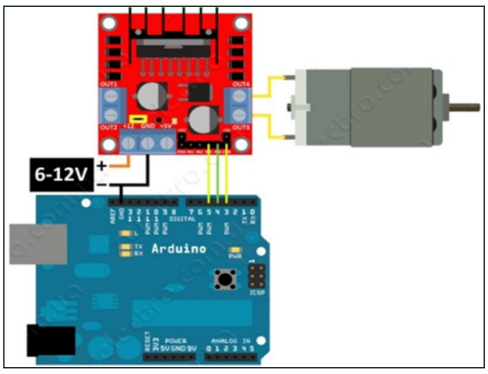

Figure 14: Measurement chain for traction motor speed

The estimation of the torque developed by the motor was performed indirectly by measuring the absorbed current, using the ACS712 sensor, which provides an analog signal proportional to the current intensity (Fig. 15). Based on the electromechanical characteristics of the DC motor, the motor torque is proportional to the armature current, according to the fundamental relationship $M_t = k_t \cdot I$, where k_t is the torque constant. The extension of the experimental system to the full configuration of the 6×6 platform involves the use of three motor drivers and three current sensors, integrated in a centralized acquisition chain based on Arduino Mega 2560, for the simultaneous monitoring of the six traction actuators (Fig. 16).

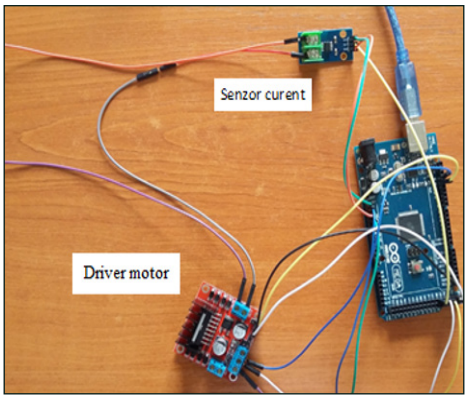

Figure 15: Measurement chain for determining the torque developed by the traction motor

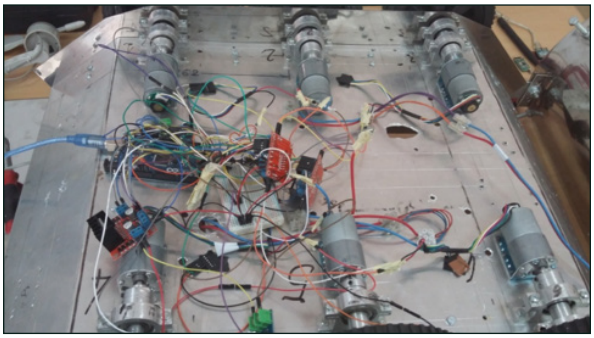

Figure 16: Measurement chain for the six motors

Experimental Results and Signal Validation

The experimental tests were carried out in longitudinal displacement mode, at constant voltage and current, for the wheels on the right side of the robot, corresponding to the front and rear axles. The position of the center of mass was considered symmetrical with respect to the rotation axes of the six motors, in order to eliminate asymmetric influences on the load distribution. The encoder signals corresponding to the tested wheels are presented in Fig. 17 and Fig. 18, highlighting the dynamics of the speed in idle operation mode.

For the right wheel of the front axle, the time required to register 20.58 revolutions was 15.3s, resulting in a speed of approximately 81rpm under no-load conditions. For the right wheel of the rear axle, the time required for 24.16 revolutions was 18.475s, corresponding to a speed of 78.6rpm. The small difference between the two values indicates the uniformity of the engine characteristics and the limited variability of mechanical losses in the integrated reduction gears, a critical aspect for uniform traction distribution in the 6×6 architecture.

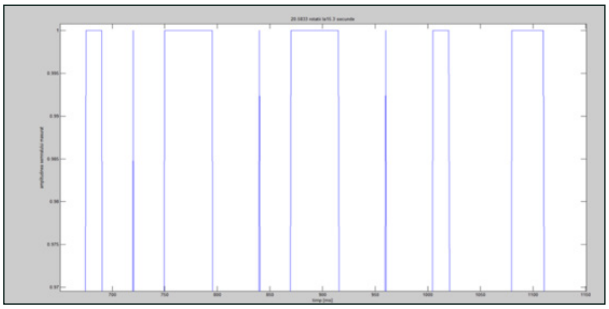

Figure 17: Encoder signal – right wheel, axle 1 (front)

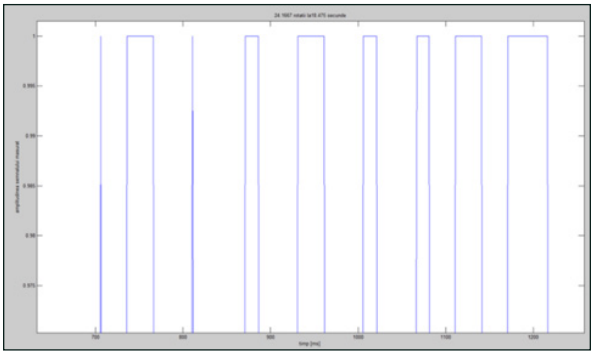

Figure 18: Encoder signal – right wheel, axle 3 (rear)

To validate the encoder signal shape and reduce uncertainties due to acquisition noise, one of the channels was monitored with an oscilloscope (Fig. 19). The rectangular signal confirms the correct operation of the incremental encoder, and the discrepancies with the software acquired signals are attributed to electromagnetic noise and resolution limitations of the acquisition system, a phenomenon well documented in the instrumentation and measurement literature.

Figure 19: Encoder signals recorded on the oscilloscope

Torque Estimation via Current Measurement

The motor torque was estimated based on the analog signal provided by the current sensor, proportional to the intensity of the current absorbed by the motor. The experimental results for the front and rear axle wheels are presented in Fig. 20 and Fig. 21, highlighting similar values of the torque developed in the no-load regime. The supply voltage was kept constant, resulting in a stable speed and a relatively constant current, which confirms the linear character of the system in the nominal regime.

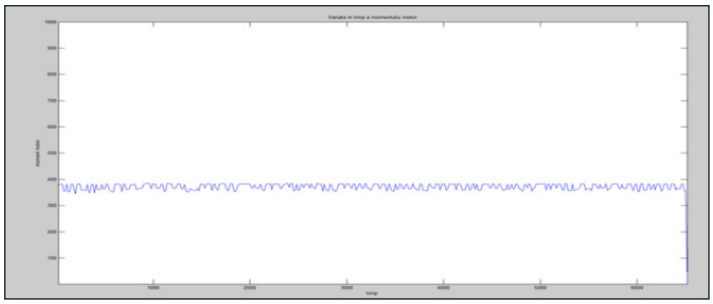

Figure 20: Variation of engine torque for the right wheel corresponding to axle 1 (front)

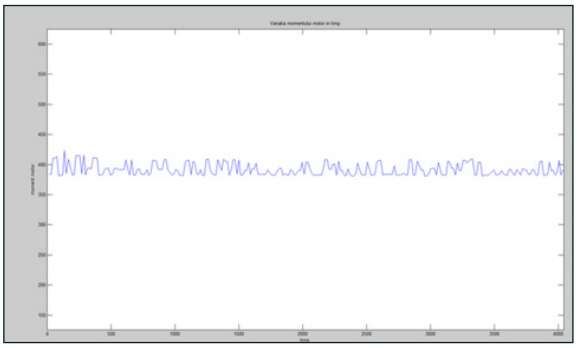

Figure 21: Variation of engine torque for the right wheel corresponding to axle 3 (rear)

The acquisition of speed data was performed with a sampling period of 15ms, imposed by the limitations of the software timer implemented in the C# environment. Although this sampling rate is sufficient for the analysis of the steady-state regime, it may limit the transient characterization of the system, suggesting the need to use acquisition methods with higher temporal resolution for advanced dynamic studies.

The conversion of the raw values provided by the analog-to-digital converter into current intensity was achieved through the relationship.

$$A = \frac{0.0049 \cdot N_{ADC} - 2.2}{0.185} \tag{28}$$

where $N_{ADC} \in [0.1023]$ represents the discrete value provided by the controller ADC, 0.0049 V is the resolution per bit for a 5 V reference, 2.2 V is the sensor output offset for zero current, and 0.185 V/A is the sensitivity of the ACS712 sensor. Applying the relationship for $N_{ADC} = 400$, a current intensity of approximately 1.3A was obtained, a value subsequently used to estimate the motor torque through the fundamental torque-current relationship.

Conclusions

The analytical and dynamic model developed for the 6×6 mobile platform confirms the compliance of the proposed architecture with the requirements of mobility, stability and operation in potentially risky environments, demonstrating the validity of the integrated theoretical-experimental approach. The analysis of the kinematic and dynamic parameters highlights the critical influence of the center of mass positioning on the

obstacle crossing capacity and on the longitudinal stability on slopes. In particular, increasing the height of the center of mass and moving it towards the front of the platform improves the performance of overcoming step-type obstacles, but induces significant compromises in terms of stability during braking on slopes and lateral loads during turning maneuvers, confirming the predictions of classical theories of terrain mechanics and vehicle stability.

The analytical-numerical and experimental results indicate that the expansion of the tire-ground contact area leads to an increase in lateral forces in the turning regime, while the widening of the contact patch reduces the average ground pressure and the depth of subsidence in deformable soils. This reduction in subsidence limits the phenomenon of lateral excavation and decreases the resistive moment in the turn, contributing to improving the maneuverability and energy efficiency of the platform. The total traction force estimated by the model and validated experimentally is sufficient for movement in terrains with reduced bearing capacity and for crossing discrete obstacles, and the geometric parameters of the designed gauge satisfy the stability criteria for dynamic turning regimes.

The limitations identified in the progression of the platform in the context of radiation detection missions highlight clear directions for future optimization of the propulsion subsystem and mechanical configuration, including mass redistribution, suspension geometry optimization and implementation of adaptive torque control strategies. The observed constructive imperfections are inherent to the nature of the laboratory prototype and do not affect the overall conclusions regarding the validity of the model, the robustness of the proposed methodology and the feasibility of implementing the platform in autonomous applications critical from the point of view of operational safety.

References

1. Lucian-Ștefăniță Grigore, Iustin Priescu, Dan-Laurențiu Grecu (2020) Artificial Intelligence Applied in Fixed and Mobile Robotic Systems, AGIR Publishing House, Bucharest.
2. Jo Y Wong (2024) Terramechanics and Off-Road Vehicle Engineering. 3rd Edition, Publisher: Butterworth-Heinemann https://shop.elsevier.com/books/terramechanics-and-off-road-vehicle-engineering/wong/978-0-443-15614-4.
3. Jo Y Wong (2001) Theory of ground vehicle. 3rd Edition, Publisher: John Wiley & Sons https://trid.trb.org/View/859982.
4. Carmen-Silvia Oprina, Ciprian Răcuciu, Lucian-Ştefăniţă Grigore (2025) Contributions Regarding the Use of Unmanned Ground Robots for Radiation Measurements. 17th International Conference on Electronics, Computers and Artificial Intelligence (ECAI), Publisher: IEEE https://ieeexplore.ieee.org/document/11095573.
5. Dénes Takács, Gábor Stépán (2013) Contact patch memory of tyres leading to lateral vibrations of four-wheeled vehicles. Philosophical Transactions of the Royal Society A: Mathematical, Physical and Engineering Sciences 371.
6. Wei Yu, Oscar Chuy Jr, Emmanuel G Collins Jr, Patrick Hollis (2009) Dynamic modeling of a skid-steered wheeled vehicle with experimental verification. IEEE/RSJ International Conference on Intelligent Robots and Systems, Publisher: IEEE https://ieeexplore.ieee.org/document/5354381.
7. Meng Wang, James NK Liu (2005) Fuzzy logic based robot path planning in unknown environment. International Conference on Machine Learning and Cybernetics IEEE https://ieeexplore.ieee.org/document/1527055.
8. Vahid Tavoosi, Javad Marzbanrad, Ramadan Mirzaei (2018) Vertical Dynamics Modeling and Simulation of a Six-Wheel Unmanned Ground Vehicle. International Journal of Automotive Engineering 8: 2709-2729.
9. Pekka Appelqvist, Jere Knuuttila, Juhana Ahtiainen (2010) Mechatronics Design of an Unmanned Ground Vehicle for Military Applications. Mechatronic Systems Applications, InTechOpen 237-262,
10. Jo Y Wong, CF Chiang (2001) A general theory for skid steering of tracked vehicles. Proceedings of the Institution of Mechanical Engineers, Part D: Journal of Automobile Engineering 215: 343-355
11. Rose F Millard, Raj Aggarwal, David E Aspnes, John T Feddema, J William Goodwine (2002) Technology Development for Army Unmanned Ground Vehicles. The National Academies Press 188.
12. Pedro Deusdado, Magno Guedes, André Silva,

Francisco Marques, Eduardo Pinto (2016) Sediment Sampling in Estuarine Mudflats with an Aerial-Ground Robotic Team. Sensors Journal MDPI 16.

13. Kamran H Sedighi, Kaveh Ashenayi, Theodore W Manikas, Roger L Wainwright, Heng-Ming Tai (2004) Autonomous local path planning for a mobile robot using a genetic algorithm. Proceedings of the 2004 Congress on Evolutionary Computation (IEEE Cat. No.04TH8753), Publisher: IEEE https://ieeexplore.ieee.org/document/1331052.
14. Conor Mack (2017) Machine learning fundamentals (I): Cost functions and gradient descent. Towards Data Science https://medium.com/data-science/machine-learning-fundamentals-via-linear-regression-41a5d11f5220.